J. Fluid Mech. (1998), *vol.* 359, *pp.* 143–164. Printed in the United Kingdom

Instability of thermocapillary–buoyancy convection in shallow layers. Part 1. Characterization of steady and oscillatory instabilities

By R. J. RILEY† AND G. P. NEITZEL

The George W. Woodruff School of Mechanical Engineering, Georgia Institute of Technology, Atlanta, GA 30332-0405, USA

(Received 5 October 1996 and in revised form 12 November 1997)

Combined thermocapillary–buoyancy convection in a thin rectangular geometry is investigated experimentally, with an emphasis on the generation of hydrothermal-wave instabilities. For sufficiently thin layers, pure hydrothermal waves are observed, and are found to be oblique as predicted by a previous linear-stability analysis (Smith & Davis 1983). For thicker layers, both a steady multicell state and an oscillatory state are found to exist, but the latter is not in the form of a pure hydrothermal wave.

1. Introduction

Thermocapillary convection is bulk fluid motion driven by temperature-induced interfacial-tension variations. Such flows occur in situations with liquid–liquid or liquid–gas interfaces which also experience variations in temperature. The case of interest is that of a free surface between a liquid and a passive gas. For liquids of interest here, surface tension decreases with increasing temperature, and this effect is represented by the fluid property $\gamma = -\partial\sigma/\partial T$, where σ is the surface tension and T is the temperature of the interface. Through the tangential-stress balance at the interface, surface-temperature gradients generate an interfacial shear stress which drives the surface flow in the direction opposite to that of the surface-temperature gradient. For thermally driven flows, buoyancy forces will also be present, but if the dimensions of the flow are small enough or if the flow occurs in a microgravity environment, thermocapillary forces will be dominant. Examples of such flows include the thermocapillary migration of small bubbles or droplets in a thermal field, and classical Rayleigh–Bénard convection.

Recently, there has been interest in the role of thermocapillary convection in processes such as thin-film coating and crystal growth from the melt. Specifically, in crystal-growth flows there is interest in the instability of steady thermocapillary convection, leading to oscillatory convection which results in poor crystal quality brought about by unsteady solidification at the liquid/crystal (freezing) interface (Gatos 1982). To this end there has been a large amount of research done on a model of the float-zone crystal-growth process known as the half-zone. In this model, a liquid bridge is held in place by surface-tension forces between two coaxial cylindrical rods maintained at different temperatures. Buoyancy is minimized by heating the half-zone

† Present address: Cabot Corporation, Research and Development, Pampa, TX 79066, USA.

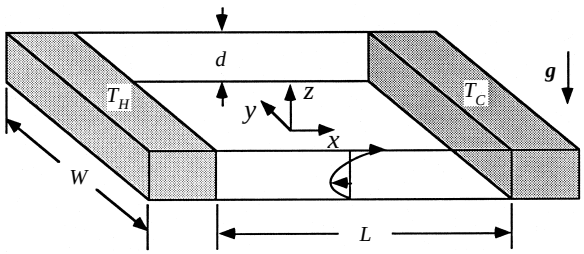

FIGURE 1. Problem geometry and coordinate specification.

at the top and cooling at the bottom to provide a stable axial-buoyancy gradient. The free surface of the liquid bridge is thus subject to a temperature gradient and the flow in the bulk is driven by the resulting thermocapillary convection.

The first documentation of oscillatory thermocapillary convection in half-zones is due to Schwabe *et al.* (1978) and Chun & Wuest (1979). Both groups measured the oscillating temperature fields in half zones with diameters of a few millimetres and found oscillations with frequencies of the order of 1 Hz. More in-depth experimental studies of oscillatory flow in half-zones can be found in the work of Preisser, Schwabe & Scharmann (1983) and Velten, Schwabe & Scharmann (1991). Recent theoretical work on the half-zone problem has been performed by Shen *et al.* (1990), Neitzel *et al.* (1991, 1993), Wanschura *et al.* (1995) and Levenstam & Amberg (1995). The first two of these studies employ energy-stability theory, the next pair, linear-stability theory, and the final one, direct numerical simulation of a model half-zone problem. The results of the various theoretical approaches are in agreement with each other and in reasonable agreement with available experimental results (see e.g. Velten *et al.* 1991)) on half-zones.

The flow examined in this work is that of a thin liquid layer of depth d in a horizontal, rectangular slot driven by both thermocapillary and buoyancy forces as shown in figure 1. This flow possesses some of the central features of the half zone such as a return-flow basic state, a velocity profile for which is sketched in the figure. The geometry allows for very large aspect ratios L/d and W/d to minimize the effects of endwalls and sidewalls, respectively. By changing the depth of the layer, control over the influence of buoyancy is also possible. A temperature gradient is produced on the free surface by maintaining a temperature difference $\Delta T = T_H - T_c > 0$ between the two endwalls; the sidewalls and bottom are assumed adiabatic. Since $\gamma > 0$, the thermocapillary stress pulls the free surface from the hot wall to the cold wall. Buoyancy also serves to drive the flow in the same direction as thermocapillary forces, but the case of greatest interest in this study is that for which thermocapillary effects are dominant, implying thin liquid layers.

The strength of thermocapillary convection is characterized by the Marangoni number,

$$Ma_L = \frac{\gamma d^2 \Delta T}{\mu \alpha L}, \tag{1}$$

where μ is the dynamic viscosity, α is the thermal diffusivity, and L is the streamwise domain length indicated in figure 1. This definition facilitates the comparison of experimental results from different length slots, since the driving force for the flow is $\Delta T/L$; however, it differs from that used in theoretical treatments for layers of

infinite horizontal extent, i.e.

$$Ma = \frac{\gamma d^2 \, \partial T/\partial x}{\mu\alpha}, \tag{2}$$

which employs the temperature gradient along the interface. We shall refer to the quantity defined in (1) as the *laboratory* Marangoni number, and indicate it by the L subscript. Owing to the existence of thermal boundary layers near both the hot and cold walls, $Ma_L > Ma$, where the value of $\partial T/\partial x$ employed in (2) is that in the interior, 'core' region, of the flow, where the surface-temperature variation is nearly linear. The definition of Ma provided in (2) permits easier comparison with available theory for infinite layers, but requires an *a posteriori* measurement of $\partial T/\partial x$. If one believes that the instability of this core flow is responsible for observed oscillations in very thin layers and that end effects serve merely to modify these, then Ma is the true Marangoni number of interest since it is apparatus-independent. As layer depth d decreases for fixed L (see figure 1), the core region of the flow exhibits a more nearly linear variation of surface temperature with streamwise distance. Consequently, as $d/L \to 0$, we expect better agreement between experiment and theory due to the existence of a more linear thermal field and also to the reduced effect of the endwalls on the core velocity field.

Buoyancy effects can be quantified in terms of the dynamic Bond number,

$$B_{0_D} = \frac{\rho g \beta d^2}{\gamma}, \tag{3}$$

which is a measure of the relative strength of buoyancy forces to thermocapillary forces. Here ρ is the density, g is the gravitational acceleration, and β is the thermal-expansion coefficient. The dynamic Bond number can be formed as Ra/Ma, where Ra is a Rayleigh number which uses the same horizontal ΔT as the Marangoni number.

Also of importance in these flows is the Prandtl number, $Pr = \nu/\alpha$, where ν is the kinematic viscosity. The Prandtl number for the liquid used in this study is $O(10)$, which implies a strong coupling between the thermal and momentum fields. Either of the Marangoni numbers defined above may be expressed as the product of the Prandtl number and a corresponding Reynolds number, i.e. $Ma_L = Re_L Pr$ or $Ma = RePr$.

Since the thermocapillary-driven surface flow in the closed domain of figure 1 creates a pressure gradient to drive the return flow, the normal-stress boundary condition on the free surface requires a non-zero surface curvature (Davis & Homsy 1980). However, in the limit of infinite mean surface tension the surface becomes flat, and hence a constant-depth thermocapillary slot flow as sketched in figure 1 is possible. Two dimensionless groups that indicate the amount of surface deflection are the surface-tension number

$$S = \frac{\rho d \sigma}{\mu^2}, \tag{4}$$

and the capillary number,

$$Ca = \frac{\mu U}{\sigma}. \tag{5}$$

A flat free surface is achieved if $S \to \infty$, and $Ca \to 0$. In the present experiments, S and Ca are typically of the order of 25 000 and 0.001, respectively, indicating that the assumption of a flat free surface is reasonable.

Pure thermocapillary convection and its counterpart including buoyancy have received attention from both theoreticians and experimentalists. Sen & Davis (1982) computed states of steady two-dimensional thermocapillary flow in slots, including

free surface deformation. Smith & Davis (1983) investigated the stability of a return-flow basic state in the core of such a slot to convective instabilities, finding a new form of instability which they termed a *hydrothermal wave*. This mode is a temperature-disturbance wave that propagates in a direction which depends on the liquid's Prandtl number. For small Pr, the waves propagate transversely across the layer and for large Pr the direction is nearly opposite that of the surface flow. For intermediate Pr, the hydrothermal waves are predicted to propagate obliquely against the surface flow, and this behaviour is the expected one for the experiments presented in this paper. The physics of the instability mechanism were later elucidated by Smith (1986) for the small- and large-Pr limits in terms of the interaction between the thermal field and the inertially (low Pr) or viscously (high Pr) dominated flow field. For the Prandtl number (approximately 14) of the liquid used in these experiments, the high-Pr mechanism is the more relevant one. In this limit the hydrothermal-wave instability is sustained by the coupling between the convection of thermal disturbances by the basic-state velocity field, and conduction of these disturbances to create new instability-initiation spots. Extension of the Smith & Davis theory to account for the influence of buoyancy forces has been done by Garr-Peters (1992*a, b*), Parmentier, Regnier & Lebon (1993) and Mercier & Normand (1996).

Kirdyashkin (1984) was the first to analytically investigate combined thermo-capillary–buoyancy-driven flow in a thin two-dimensional slot in the core region away from the endwalls. He presents both velocity and temperature profiles, and also includes experimental results obtained using ethyl alcohol in a 900 mm slot with a typical layer depth of 10–20 mm. Steady-state profiles are fully developed in the core region, agreeing well with analytical solutions. A parallel-flow core region is typically observed in the middle 90% of the domain, with endwall influence extending approximately three layer depths from each wall.

Villers & Platten (1992) conducted experiments and performed two-dimensional numerical simulations of combined thermocapillary–buoyancy flow in a thin layer of acetone ($Pr = 4.2$). A central finding of their work is that, as the Marangoni number increases, the flow transitions from a single steady convection cell, to multiple steady cells, and then to an oscillatory state with oscillation periods on the order of 5 s. De Saedeleer *et al.* (1996) have performed more recent experiments in decane ($Pr = 15$), observing also that the first transition is to a steady multicellular state. We shall see from the present results that a combination of buoyancy and geometric factors are likely to be responsible for this deviation from the Smith & Davis (1983) transition scenario.

Schwabe *et al.* (1992) have documented similar behaviour in slot and annular-pan geometries employing layer depths of ethanol ($Pr = 17$) on the order of a few millimetres. Here, multiple steady multicellular structures are also observed. Transition Marangoni numbers for the various regimes are determined; that from a single steady cell to multiple steady cells occurs for $Ma > 600$, and the transition from multiple steady cells to an oscillatory state is observed for $Ma > 3000$. Most of the reported results are for the annular-pan geometry, for which no theoretical results are presently available. Schwabe *et al.* (1992) report two different types of oscillatory flow states, depending on the layer depth: for $d < 1.4$ mm, a short-wavelength azimuthally travelling state is seen, while, for $d > 1.4$ mm, a long-wavelength state with a radially propagating component is observed. Results of the present work could imply that the difference between these two states may be related to an effect of the dynamic Bond number. Unfortunately, very few results are reported for the rectangular geometry, which is very similar to that employed for the present experiments. Those which are

provided are for the single layer depth of 1.8 mm, which is likely to be too deep to observe pure hydrothermal waves, as will be noted later.

The primary aim of the experiments described in this work is to examine combined thermocapillary–buoyancy convection in thin horizontal layers, with the goal of observing a pure hydrothermal-wave instability. This has been successfully accomplished. Since this instability is believed to be responsible for the degradation of material grown via the float-zone process, the possibility of eliminating such oscillations is of interest. In Part 2 (Benz *et al.* 1998), the feasibility of suppressing hydrothermal waves through active periodic heating of lines on the free surface is demonstrated for the moderate-Pr liquid used in these experiments. However, it must be emphasized that the hydrothermal-wave instabilities which occur in a liquid of moderate Prandtl number are driven by a different mechanism (Smith 1986) from that responsible for similar instabilities in low-Prandtl-number liquids characteristic of liquid metals.

2. Experimental setup and techniques

2.1. *Working liquid and apparatus*

The working fluid used in these experiments is 1 cS Dow Corning silicone oil. It has the desirable properties that it is transparent to visible light, allowing both flow visualization and quantitative measurement using laser-Doppler velocimetry (LDV), and has a free surface which is relatively resistant to contamination. In addition, we shall examine the spanwise structure of the observed instabilities by visualizing the thermal field of the free surface using an infrared camera. The chosen oil also has an absorption band in the infrared within the detectable wavelength range of this camera which is strong enough to allow infrared visualization of the liquid's surface temperature rather than that in the bulk.

The Prandtl number of the silicone oil used here is $Pr = 13.9$, indicating that the thermal field is strongly coupled to the velocity field and, according to the theory of Smith & Davis (1983), the preferred instability should be a hydrothermal wave. The properties of the oil, coupled with the thin layers investigated here ($O(1$ mm$)$), also ensure that the free surface of the layer is flat. A fluid possessing a low vapour pressure is also desirable in thermocapillary flow experiments due to the likelihood of evaporation at the hot end of the apparatus. The 1 cS oil was chosen after experimenting with silicone oils with viscosities in the range of 0.65–10 cS in part because it was found to have the fewest problems with evaporation.

The test cell was designed with the goal of observing a hydrothermal-wave instability; a schematic of the cell is shown in figure 2. The length L and width W of the flow section are 30 mm and 50 mm, respectively; for the range of layer depths examined in this work, these choices afford streamwise (x-direction) and spanwise (y-direction) aspect ratios of $12 \leqslant L/d \leqslant 40$ and $20 \leqslant W/d \leqslant 67$, respectively. These permit both the establishment of a well-developed return-flow velocity profile in the core region away from the walls and the accommodation of a relatively large number of hydrothermal waves. For a liquid with $Pr = 13.9$, the linear-stability analysis of Smith & Davis (1983) predicts a most-dangerous disturbance with a wavelength of approximately $2.4d$, propagating upstream at an angle of 20° to the streamwise direction of the basic state. Thus, at least a dozen hydrothermal waves can exist in the domain, and the large spanwise extent of the apparatus allows minimized impedance in the oblique propagation direction.

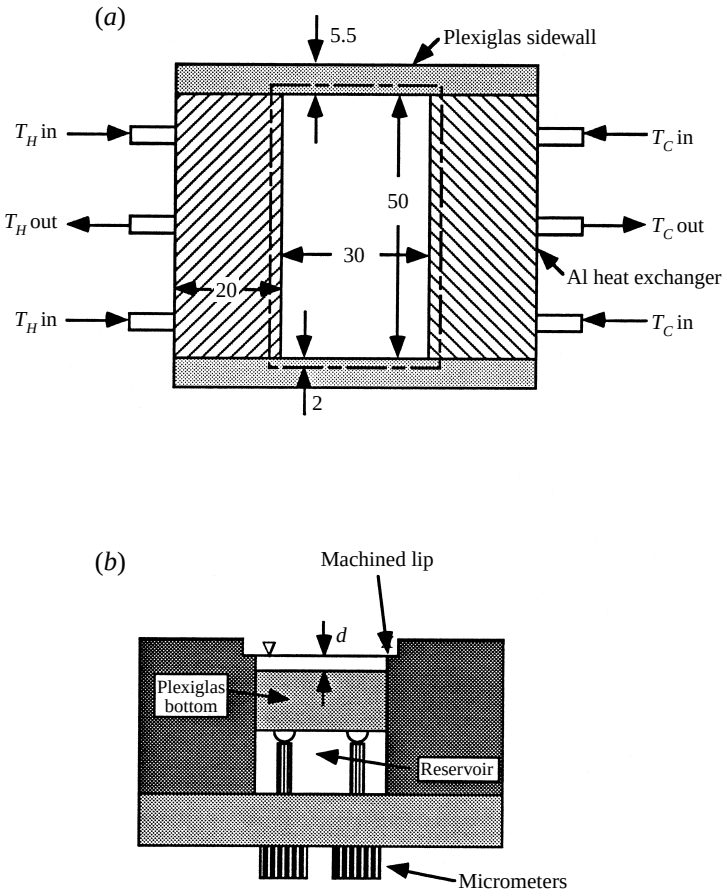

FIGURE 2. Experimental apparatus schematic (all dimensions are in mm): (*a*) top view; (*b*) side view.

To provide an accurate determination of the depth d and its continuous variability, the apparatus was designed with a movable base and reservoir, as seen in the side view of figure 2(*b*). The base is a machined Plexiglas block which fits snugly within the cavity created by the endwalls and sidewalls, yet has very small gaps (O(0.025 mm)) between it and the vertical walls which permit the addition of liquid to the layer through the reservoir. Three ball bearings mounted in the underside of the base ride on micrometers, allowing depth adjustment of the flow domain to within 0.005 mm. The apparatus is filled by injecting silicone oil into the reservoir, as suggested above. The sidewalls are also constructed of Plexiglas in order to approximate adiabatic boundary conditions. The endwalls, through which temperature-controlled water is circulated, are aluminium to provide uniform constant-temperature boundary conditions at both endwalls. Endwall temperatures are measured directly using thermocouples mounted in the centre of each endwall a distance of 1 mm from the surface which is in contact with the oil. The difference in endwall temperatures is able to be resolved to within 0.05 °C.

In order to achieve a definite and repeatable layer depth without a meniscus, a 90°, 2 mm lip has been machined along the top of the sidewalls and endwalls which serves to pin the contact line of the silicone oil. The upper surface of this lip is coated with

a fluorad (3M Scotchguard) surface-modifying treatment, which inhibits the liquid from wetting the lip. The existence of this lip with a pinned contact line is crucial to the establishment of a layer of uniform depth. Levelling of the apparatus is achieved by mounting it on a three-point micrometer-type tilt table. Adjustments to the tilt are made while observing the reflections of a grid in the free surface near the lip regions, and continue until the grid appears undistorted at all points along the lip, indicating a flat free surface. Isolation from laboratory vibrations is achieved by securing the tilt table to a commercial vibration–isolation table.

Two approaches were investigated for minimizing disturbances at the free surface due to transient laboratory air currents. The first was to cover the apparatus with a Plexiglas lid allowing a 5 mm thick gas layer above the free surface. However, this method experienced problems with condensation of trapped silicone-oil vapour at the cold wall. The formation of droplets on the cold horizontal lip ultimately results in the loss of the pinned contact line, requiring the cessation of experiments and the cleaning and re-coating of the apparatus. An alternative technique was successful, however. A Plexiglas shroud 60 mm $\times$ 60 mm in cross-section and 100 mm in height was placed around the flow cell. Since the upper end of the shroud was open to the laboratory, over time liquid depletion due to evaporation results in a change in the position of the free surface. Although the rate of evaporation is quite small ($O(0.1\ \mu l/s)$), the resulting depth change is unacceptable for these experiments. Hence, the evaporating silicone oil was replaced by liquid supplied from a constant-head container to the reservoir at the required rate. At the typical re-supply rate, the effective vertical velocity at the free surface is roughly 0.07 $\mu m\ s^{-1}$ or about 0.001% of the measured free-surface speed, and is therefore felt to have a negligible impact.

Properties of the Dow Corning 200, 1 cS silicone oil used in these experiments were obtained from the manufacturer, with the exception of the surface tension. These data were measured directly by colleagues at the Microgravity Advanced Research Support (MARS) Center in Naples, Italy using the wire loop method for the range of the temperatures encountered in the present experiments. From these measurements, a linear least-squares fit of the data yielded the result

$$\sigma(T) = 17.237 - 0.0755(T - T_0)\ \text{mN m}^{-1} \tag{6}$$

where $T_0 = 25\ ^\circ\text{C}$ was the reference temperature about which experiments were performed.

2.2. *Experimental techniques*

Four different experimental techniques were used to explore the flow states encountered in this work. Quantitative measurements of steady-state velocity fields, both prior to and subsequent to the onset of instability, were performed with a TSI single-component LDV. The flow was seeded with dilute amounts of silicon-carbide particles with a mean diameter of 1.5 μm. Velocity-profile measurements through the depth (z) of the layer allow one to see the degree to which the assumed return-flow basic state is achieved; measurements as a function of streamwise (x) and spanwise (y) distance permit an assessment of the influences of endwalls and sidewalls, respectively.

Flow-visualization experiments were performed using two techniques. For the first, the flow was seeded with polystyrene microspheres with diameters ranging from 1–15 μm and these were observed within a 1 mm thick laser-sheet illumination of an (x, z)-plane. A Dage-MTI CCD camera was used to record the resulting images for both steady and unsteady flow conditions. Since the particles were slightly more dense than the test liquid, problems were experienced with keeping the particles from

settling to the bottom. In a static fluid, particle settling time through the depth of the layer (at 10 μm s^{-1} for an average 8 μm particle) is roughly two minutes; for dynamic experiments, particles remain in suspension longer, but insufficiently long for the method to be useful for extended periods of time. The second technique employed was shadowgraphic visualization across (i.e. in the y-direction) the layer. Thermally induced index-of-refraction variations, integrated through the span of the layer, were likewise recorded using the CCD camera. While no attempt was made to extract quantitative data from these results, the shadowgraphic technique is quite sensitive, providing clear indications of both the existence of multicellular structures and unsteadiness. It is the visualization method of choice for pinpointing the flow transitions to be reported in §3. The only limitation of the technique, with regard to the present experiments, is the fact that the mean temperature gradient bends the light downward on its way to the camera so that, at some limiting depth, it is no longer possible to obtain clean shadowgraphic images of the flow. For this apparatus and the conditions of these experiments, this limiting depth is 0.75 mm.

The final technique used in these experiments was infrared thermography of the free surface. The use of this technique was central to the investigation of oblique hydrothermal-wave instabilities and to the suppression of these waves reported in Part 2. In addition, it permits the observation of the structure of the multicellular instability and its subsequent transition to oscillatory flow. These measurements were performed using an Amber AE-4128 infrared camera employing a 128×128 element indium-antimonide focal-plane-array detector, which is sensitive to radiation in the range of 1–5.5 μm. The output from the camera was captured with a variable-scan frame grabber mounted in an IBM-compatible 386 computer, allowing it to be displayed on a video monitor or recorded onto video tape. Further details on this and all other techniques employed in these experiments may be found in Riley (1995).

3. Results

The combination of methods described above was used to investigate the flow structures observable in the test cell over a range of conditions which was as large as possible, given the inevitable constraints imposed by the apparatus, test liquid and measurement techniques, some of which are described above. The results to be presented here will focus on the return-flow basic state, its instability to both hydrothermal waves and to a steady multicellular state, and the onset of time-dependent flow from the steady multicellular state. The transition map for the states observed is presented in terms of the laboratory Marangoni number Ma_L (equation (1)), and true Marangoni number Ma (equation (2)) in figure 3.

There are three major categories into which the observations fall: steady, unicellular flow (SUF); steady multicellular flow (SMC); and oscillatory flow. The last of these categories, however, may be further divided depending on whether the state preceding the onset of oscillatory flow was unicellular (leading to the hydrothermal waves (HTW) predicted by Smith & Davis 1983) or multicellular (leading to oscillating multicellular flow (OMC)). It should be pointed out that, while we have chosen to characterize the transitional Marangoni numbers in terms of the dynamic Bond number, there is the additional possible dependence of the transition sequence on the two aspect ratios L/d and W/d. Since this apparatus does not allow these to be held constant as the depth of the layer is varied, it is not possible to unequivocally attribute the observed transition to multicellular flow to a particular effect.

As noted in §1, Ma_L exceeds Ma, owing to the existence of thermal boundary

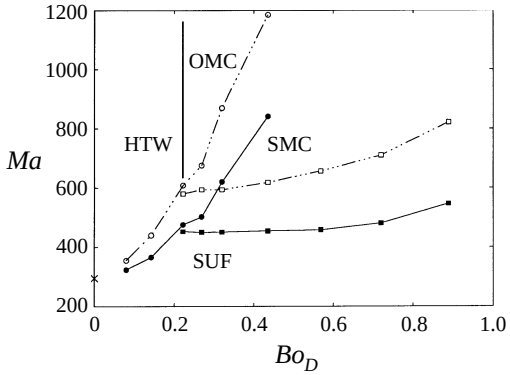

FIGURE 3. Transition map of the experimental results in terms of Ma_L (open symbols) and Ma (closed symbols) for transitions to hydrothermal waves (HTW), steady multicells (SMC) and oscillating multicells (OMC). The single × plotted on the ordinate corresponds to the linear-theory result of Smith & Davis (1983) for the onset of hydrothermal waves.

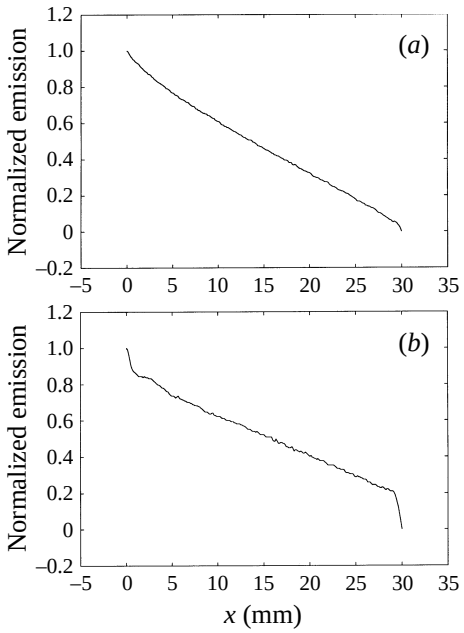

FIGURE 4. Normalized IR camera emission for the steady unicellular state (just prior to onset) along the streamwise coordinate in the centre of the span for a layer of (*a*) 0.75 mm thickness; and (*b*) 2.5 mm thickness.

layers at the temperature-controlled endwalls, particularly for moderate-to-high-Pr liquids such as the one employed here. These boundary-layer effects become more pronounced as the layer depth increases, as seen in figure 4, which shows a normalized emission from the IR camera along a line in the middle of the span of the layer as a function of streamwise distance x for two different layer depths. For both cases in figure 4, the emission profiles correspond to a state of steady unicellular flow just prior to the appearance of either hydrothermal waves (figure 4*a*) or steady multicellular flow (figure 4*b*).

In order to correct the Marangoni number for this effect, the emission data in

d (mm)	Bo_D	Ma_L (HTW)	Ma (HTW)	Ma_L (SMC)	Ma (SMC)	Ma_L (OMC)	Ma (OMC)
0.75	0.080	355	324	n.o.	n.o.	n.o.	n.o.
1.00	0.142	440	366	n.o.	n.o.	n.o.	n.o.
1.25	0.222	609*	476*	580	453	n.o.	n.o.
1.375	0.269	n.o.	n.o.	595	451	677	503
1.50	0.320	n.o.	n.o.	595	452	871	621
1.75	0.435	n.o.	n.o.	619	455	1185	842
2.00	0.569	n.o.	n.o.	658	459	n.i.	n.i.
2.25	0.720	n.o.	n.o.	711	482	n.i.	n.i.
2.50	0.889	n.o.	n.o.	822	547	n.i.	n.i.

TABLE 1. Transitional Marangoni numbers versus depth and dynamic Bond number for transitions to hydrothermal waves (HTW), steady multicells (SMC) and oscillating multicells (OMC). The asterisks mark a case which is not a true transition to HTW, n.o. denotes not observed, and n.i. not investigated.

the interior region of the flow, i.e. $5 \leqslant x \leqslant 25$ mm, are fit with a straight line, which, along with the calibration data (including the known measured temperatures of the endwalls), is used to extract $\partial T/\partial x$ for the core region. This same procedure is employed for determining the core temperature gradient used to correct the transition map for the steady $\rightarrow$ oscillatory multicellular regime as well, although the data in this case are of the type seen in figure 10(*a*). In all cases, the temperature gradient is determined for a state just prior to the onset of the transitional state. De Saedeleer *et al.* (1996) also recognized the importance of determining the core temperature gradient, which they did using a thermocouple inserted below the free surface.

One advantage to the present method for determining the true temperature gradient $\partial T/\partial x$ occurring in the core of the layer is that there is no need to determine the effective emissivity of the liquid or to calibrate the grey-level values against a blackbody emission source. By taking the ratio of the linear fit to the grey-level data in the core to the gradient represented by the maximum and minimum grey levels occurring at the endwalls of the same data, the absolute values of the free-surface temperature need not be determined.

Since the determination of Ma requires an *a posteriori* measurement of the core surface-temperature distribution, this was not necessarily done for cases not associated with transitions between states. Rather, the more convenient laboratory Marangoni number Ma_L is reported in the following sections when comparing to specific experimental cases. The transitional values of both Marangoni numbers are reported as a function of both the dimensional depth and dimensionless Bo_D in figure 3 and table 1.

3.1. *Steady unicellular flow*

Of interest in characterizing this state is determining the degree to which the apparatus utilized for these experiments permits the establishment, in the core region away from vertical boundaries, of the return-flow basic state assumed in the theoretical analysis of Smith & Davis (1983). To this end, detailed LDV measurements have been performed for two states. The first case, with $(Ma_L,\ Bo_D) = (350,\ 0.142)$ corresponds to a layer of 1.0 mm depth at a Marangoni number which is 80% of the value at which transition to the hydrothermal-wave state was observed. The second case, with $(Ma_L,\ Bo_D) = (475,\ 0.320)$, is for a 1.5 mm layer depth, which first experiences a

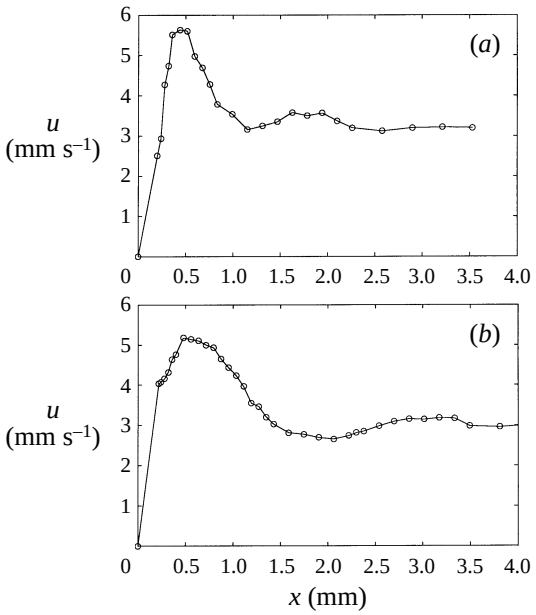

FIGURE 5. Horizontal 'surface' velocity near the hot wall: (*a*) $d = 1.0$ mm; (*b*) $d = 1.5$ mm.

transition to steady multicellular flow. The chosen Marangoni number is the same fraction (80%) of the transition value to the new state as for the first case.

Figures 5 and 6 show the variation of the x-component of 'surface' velocity near the hot and cold walls, respectively, for the two cases. These measurements were performed with the LDV fibre-optic head oriented above the layer, looking downward. It is estimated (Riley 1995) that the centre of the measurement volume (an ellipsoid with a major axis of 120 μm) is roughly 60 μm below the free surface. Measurements for both hot walls show an overshoot of the core velocity followed by an equilibration which takes place within a distance $x/d = 3$ in both cases. At the cold walls, no such overshoot is observed and the effect of the endwall is constrained to a region of approximately $x/d = 2/3$ in length.

It is possible that the observed overshoot and recovery at the hot wall are due to the formation of a strong roll cell there, in some sense a precursor to the steady multicellular state to be discussed in §3.3. Such a cell was observed even for low-Bo_D cases at Marangoni numbers immediately preceding the transition to hydrothermal-wave instability. The overshoot in velocity is consistent with LDV measurements and calculations performed by Villers & Platten (1992) for flows of acetone ($Pr = 4.24$) in containers of modest aspect ratio.

Another numerical study which has relevance to the endwall region velocity measurements is that of Ben Hadid & Roux (1990), who performed numerical calculations of thermocapillary convection in a long horizontal layer for a low-Prandtl-number fluid. Since Pr is assumed to be small, the momentum and thermal fields are decoupled, and the case of a constant applied shear stress at the free surface was considered. Thus, there are significant differences between this work and the high-Pr situation considered presently. One of the cases computed by Ben Hadid & Roux has an aspect ratio $L/d = 25$, which is comparable to the present 1 mm and 1.5 mm layers which have $L/d = 30$ and 20, respectively. For the lowest-Reynolds-number case ($Re = 66.7$) presented by Ben Hadid & Roux, the free-surface velocity increases

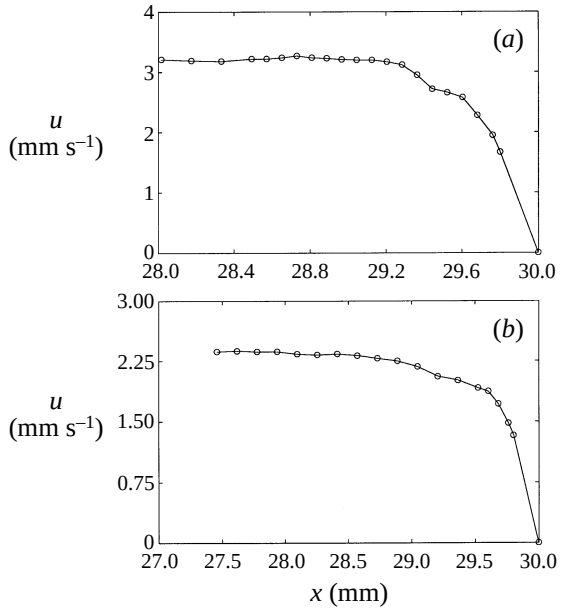

FIGURE 6. Horizontal 'surface' velocity near the cold wall: (*a*) $d = 1.0$ mm; (*b*) $d = 1.5$ mm.

monotonically away from the hot wall and decreases in a similar fashion near the cold wall, exhibiting no overshoot at either end of the slot, contrary to what has been observed in the present experiments, although this is expected in light of the free-surface conditions assumed in the calculations. The two experimental cases under discussion correspond to Reynolds numbers of $Re = 23.4$ and 34.1, respectively, for the 1.0 mm and 1.5 mm layer depths.

Measurements of surface velocity (similar to those of figures 5 and 6) made in the vicinity of the adiabatic sidewalls indicate that the free-surface velocity reaches its core value much more rapidly than observed near the heated endwalls (Riley 1995). For the cases examined, this adjustment at the streamwise centre of the layer takes place within a single layer depth.

In the core region, away from both endwalls and sidewalls, LDV measurements made through the layer indicate the degree to which the return-flow basic state is attained. The quadratic profile of Smith & Davis (1983) is modified by the existence of buoyancy. Solution of the two-dimensional Boussinesq equations for fully developed flow in the core yields the horizontal velocity,

$$U(z) = \tfrac{3}{4}z^2 - \tfrac{1}{2}z + Bo_D\left(-\tfrac{1}{6}z^3 + \tfrac{5}{16}z^2 - \tfrac{1}{8}z\right), \tag{7}$$

where length has been scaled by the depth d and velocity by the thermocapillary velocity

$$U_s = \frac{\gamma(\partial T/\partial x)d}{\mu}. \tag{8}$$

Figure 7 shows measured and theoretical profiles of $U(z)$ for the two layers considered in this section. Measurements were performed by having the two intersecting beams of the LDV enter the flow field through one of the adiabatic sidewalls. This orients the major axis of the ellipsoidal measurement volume normal to the z-direction in which the largest velocity gradients occur. Velocity-gradient broadening is there-

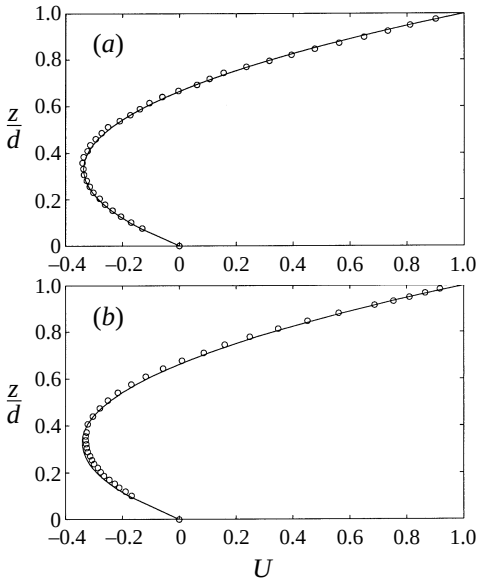

FIGURE 7. Basic-state velocity profiles for: (*a*) $d = 1.0$ mm, $Ma = 350$; open circles, LDV measurements; solid line, theory for $Bo_D = 0$; (*b*) $d = 1.5$ mm, $Ma = 475$; open circles, LDV measurements; solid line, theory for $Bo_D = 0.32$.

fore confined to the 40 μm waist dimension of the measurement volume. In order to obtain data near the bottom (free surface) of the layer, the plane of the beams entering through the sidewall is angled slightly downward (upward) to position the measurement volume as close as practicable to the location of interest. Near the free surface, where the uncertainty in the measurement is largest, the size of the standard deviation in the dimensional velocity for the 1.0 mm layer of figure 7(*a*) is $O(0.2\ \text{mm s}^{-1})$, compared with a maximum measured speed of roughly 4 mm s^{-1}. In the cases shown in figure 7, the velocity has been scaled by its maximum value at the free surface, as opposed to the thermocapillary velocity scale. For the thinner layer, the comparison between the measurements and theory is made for $Bo_D = 0$, indicating the degree to which this layer conforms to the theoretically assumed basic state of Smith & Davis (1983). In both cases, the comparison between measured data and theoretical profiles is excellent.

One final question regarding the unicellular state observed in these experiments is the degree to which flow in the core region is independent of the x-direction of figure 1. In order to assess this, measurements of the maximum value of the interior (backflow) velocity were performed at several locations between the two heated endwalls, as shown in figure 8. The points displayed as circles are all scaled using a constant value of U_s (equation (8)) corresponding to the conditions at the rightmost cold point, where the properties are computed using a conduction solution for the temperature. These data indicate the existence of a fair amount of variation between the endwalls. Speculating that a large part of this variation may be due to the temperature dependence of viscosity, we have adjusted the velocities depending on the local value of U_s, computed using the same conduction solution for temperature. The adjusted values, shown in figure 8 as squares, show much less variation, lending some credence to the hypothesis.

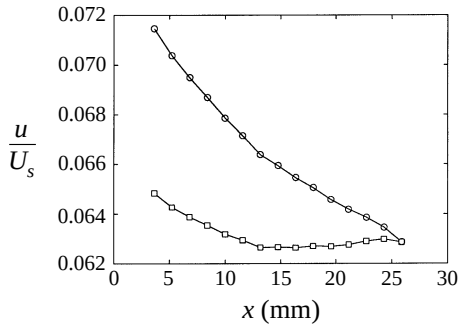

FIGURE 8. Maximum measured backflow velocity versus streamwise distance: circles, scaled by a constant U_s; squares, scaled by $U_s[T(x)]$, where T is obtained from a conduction solution.

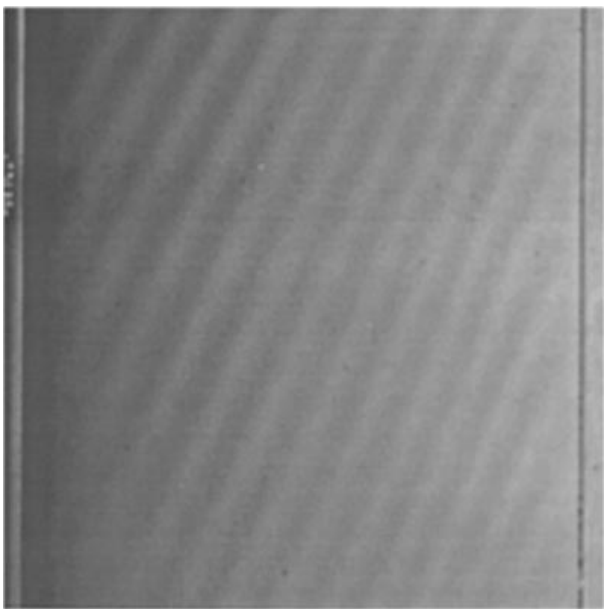

FIGURE 9. Instantaneous thermograph of hydrothermal waves on a 1.0 mm deep layer, viewed from above. The hot and cold walls are at the left- and right-hand sides of the figure, respectively, and the hydrothermal waves are propagating from lower-right to upper-left.

3.2. *Hydrothermal waves*

The state of greatest interest in the present experiments is that which results from instability of the unicellular basic state at low values of the dynamic Bond number. These hydrothermal waves are travelling thermal waves which, for the Prandtl number of the liquid used in these experiments, propagate obliquely, with a component which opposes the direction of free-surface motion. For $Pr = 14$ and $Bo_D = 0$, the theory of Smith & Davis (1983) predicts a wavelength of approximately $2.5d$ and a propagation angle $\Psi \approx 20^\circ$ with respect to the negative x-direction. In these experiments, the hydrothermal-wave transition is observed for $Bo_D \leqslant 0.22$, corresponding to layer depths $d \leqslant 1.25$ mm.

The onset of time-dependence in this case is an especially sharp one to which the shadowgraphic visualization technique is particularly sensitive. The qualitative stucture of the flow, when viewed from above with infrared thermography is clearly

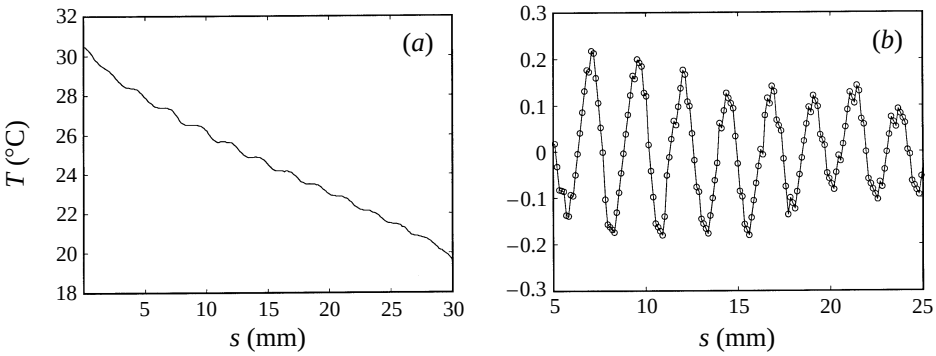

FIGURE 10. Instantaneous total temperature (*a*) and deviation from the local mean (*b*) along a line perpendicular to hydrothermal wave fronts.

in agreement with that predicted by Smith & Davis (1983). This is shown in figure 9 for a layer of 1.0 mm depth at a condition which is slightly supercritical. In accordance with the nonlinear theory of Smith (1988), only one of the two possible families of hydrothermal waves is observed. If the apparatus is level and the base and free surface are parallel (which is essential to the attainment of this state), either of these families may appear. It is clear from this thermograph that the hydrothermal waves completely fill the domain with little influence from the endwall boundaries. The same is true of the sidewall boundaries, as well, although not observable in this figure; they are constructed from Plexiglas, and hence behave as nearly adiabatic boundaries. Although very difficult to observe in figure 9, there does exist a single steady roll cell located at (and parallel to) the hot wall toward which the hydrothermal waves propagate. This cell is consistent with its appearance even in the states which have been termed unicellular. It is also apparent from the figure that the wavelength increases slightly as the waves propagate across the layer from the cold wall to the hot one. This could be a ramification of the fact that the core flow is changing with x due to the temperature dependence of viscosity, as discussed earlier, or the fact that the wavelength depends on the Prandtl number, which also varies locally with the temperature.

The temperature perturbations associated with these hydrothermal waves may be obtained from the infrared camera data. Figure 10 shows both the temperature variation (figure 10*a*) and perturbations (figure 10*b*) obtained by subtracting the mean-temperature variation along a line perpendicular to the wave fronts for data extracted from the thermograph of figure 9. From these data, it is seen that the amplitude of the temperature perturbation is not constant, but increases in the direction of propagation from roughly 0.2 °C to 0.35 °C peak-to-peak.

The structure of the hydrothermal-wave instability is quantified in terms of wavelength λ, frequency f, wave speed c, and angle of propagation Ψ for the three cases examined in this work. All of the quantities were extracted from the infrared images of the free-surface temperature fields at values of ΔT slightly above critical. Dimensional values of these quantities are presented in table 2; dimensionless values of λ, f and c are given in table 3, where wavelength has been scaled by depth, wave speed by the thermocapillary velocity scale U_s (equation (8)) and frequency by U_s/d. The dimensionless wavelength is seen to be comparable to the value $\lambda/d = 2.4$ predicted by the linear-theory zero-gravity analysis of Smith & Davis (1983) and is nearly independent of the depth of the layer. The variation of the other quantities with Bo_D

d (mm)	λ (mm)	f (Hz)	c (mm s^{-1})	Ψ (deg.)
0.75	1.95	0.98	1.91	27.9
1.00	2.58	0.57	1.47	23.2
0.25	3.37	0.38	1.28	22.4

TABLE 2. Dimensional wavelength, frequency, phase speed and propagation angle as a function of layer depth for hydrothermal-wave cases.

Bo_D	λ/d	fd/U_s	c/U_s
0.080	2.60	0.0236	0.0614
0.142	2.58	0.0217	0.0561
0.222	2.70	0.0174	0.0469

TABLE 3. Scaled wavelength, frequency and phase speed as a function of dynamic Bond number for hydrothermal-wave cases.

is more substantial, so that comparison with a zero-gravity theory is less appropriate. A linear-stability analysis incorporating buoyancy has been performed for the Smith & Davis problem (Riley & Neitzel 1998) and a comparison of these results with the present experimental ones is discussed in detail there. Suffice it to say here that the linear-theory critical Marangoni number, Ma_C (plotted as the symbol $\times$ in figure 3), agrees almost exactly with Ma_L for the smallest value of Bo_D measured in these experiments, and that the trend in Ma_C with increasing Bo_D is the same for both theory and experiment.

Previous researchers have measured oscillations in thin thermocapillary-driven liquid layers, but have not provided conclusive evidence of the hydrothermal-wave instability. The experiments of Villers & Platten (1992) in a thin acetone layer ($Pr = 4$) utilize one-point LDV measurements to determine whether the flow at a single point in the layer was steady or oscillatory. In this manner they map out a boundary in (Ma, Ra)-space denoting the steady/oscillatory transition. No discussion on the structure of the flow producing the oscillations is given, since their measurements do not provide that type of information. Much of their data are for relatively thick layers ($d \geqslant 2.0$ mm, $Bo_D \geqslant 0.362$), and hence the observed oscillations are probably the oscillating multicellular flows to be discussed in §3.4, rather than hydrothermal waves. The study by De Saedeleer *et al.* (1996) reports the first instability in the form of a steady structure which then transitions to an oscillatory state. However, calculation of the Bond number associated with their experiments reveals that it is in excess of three times the maximum value determined for the first transition to a hydrothermal-wave instability in the present experiments. In addition, their spanwise aspect ratio was quite small, which may have adverse effects for oblique waves.

Schwabe *et al.* (1992) discuss two different types of oscillatory thermocapillary flows in a thin annular geometry, so-called short- and long-wavelength instabilities. Their short-wavelength instability occurs in layers of $d \leqslant 1.4$ mm ($Bo_D \leqslant 0.18$), and has a wavelength of $\lambda \approx 6d$, for a 1 mm thick layer, whereas $\lambda = 2.58d$ for the 1 mm layer of the present study. The short-wavelength instability is investigated through single-point thermocouple measurements, and a shadowgraph technique that illuminates the oscillating meniscus formed at the lip of the inner wall of the annulus. The time variation of the meniscus at the lip appears wave-like, but no flow visualization in the bulk of the fluid is available. The dimensionless wave speed of the short-wavelength

instability is $c = 0.06$ for a 1 mm thick layer, which is in agreement with the value of $c = 0.056$ for the 1 mm layer of the present study. Thus, it is possible that Schwabe *et al.* did indeed observe hydrothermal waves in an annular geometry, but the evidence is not completely conclusive on this point.

Ezersky *et al.* (1993) claim to have produced hydrothermal waves in 5 cS silicone-oil layers in the range of $1.2 \leqslant d \leqslant 3.1$ mm, but results are presented only for a 3.1 mm layer. The flow is investigated using a shadowgraphic technique, and an image is presented which is reportedly of a hydrothermal wave. For a layer depth of 3.1 mm, $Bo_D \approx 1.4$, which is much too large for the generation of pure hydrothermal waves according to the present results. Ezersky *et al.* present a shadowgraph image showing a disturbance with a wavelength of $\lambda/d \approx 1.3$, which is in the range of the steady multicellular flow structure discussed in the next subsection.

In a similar study, Daviaud & Vince (1993) report an observed travelling-wave disturbance in 0.65 cS silicone oil, for layer depths of $0.8 \leqslant d \leqslant 2.5$ mm. However, contrary to the results of the present study, the angle of propagation of the waves was found to be perpendicular to the applied temperature gradient ($\Psi = 90°$). This could be due to the fact that their rectangular domain is quite large in the spanwise direction (200 mm), and relatively short in the streamwise direction (10 mm) in which the temperature gradient is applied. They also provide a graph of the critical applied-temperature difference (ΔT_{crit}) as a function of layer depth, which shows ΔT_{crit} decreasing with increasing depth for $0.8 \leqslant d \leqslant 1.4$ mm, followed by an increase for depths up to 2.5 mm. This behaviour is inconsistent with the results of the present study in which ΔT_{crit} decreases monotonically ($Ma_L \propto d^2$), and could be due to the difference in the geometries of the two flow domains.

3.3. *Steady multicellular flow*

The steady multicellular state observed at higher values of the dynamic Bond number are spanwise-uniform co-rotating rolls. Figure 11 shows the structure of this flow as observed by the three types of visualization techniques described in §2. In figure 11(*a*), a time exposure of sheet-illuminated particles clearly identifies the cellular structure and the associated saddle points in a layer of 2.0 mm depth; figure 11(*b*) shows an instantaneous snapshot of a combined shadowgraph/particle image; and figure 11(*c*) provides an overhead view of the temperature field visualized with infrared thermography. This last photograph clearly illustrates the two-dimensional nature of this flow state and the relative lack of influence of either sidewalls or endwalls.

Although it is impossible to ascertain from the thermographic image of figure 11(*c*), the strength of the cells decreases as one moves away from the hot wall. This may be observed by examining the streamwise variation of the horizontal velocity at a fixed vertical location, as shown in figure 12. This result is for a 1.5 mm layer depth at a value of $Ma_L = 800$, which is significantly higher than the steady multicellular-flow transition value of $Ma_L = 595$ for this Bo_D. Note that, even at this large temperature difference, the multicells decay rapidly in strength, vanishing at a distance of roughly $x/L = 2/3$. Also of note is the fact that the average velocity decreases when moving toward the cold wall, consistent with the earlier observation of a temperature-dependent viscosity effect.

The primary quantitative result to be obtained for this flow state, in addition to the transition Marangoni number, is the dependence of the wavelength of the multicellular state on the dynamic Bond number. This is provided in figure 13, and exhibits relatively smooth, yet significant, variation. Once again, it is not possible to determine whether these observations are due to buoyancy or aspect-ratio effects.

(*a*)

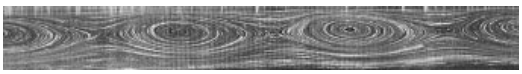

(*b*)

(*c*)

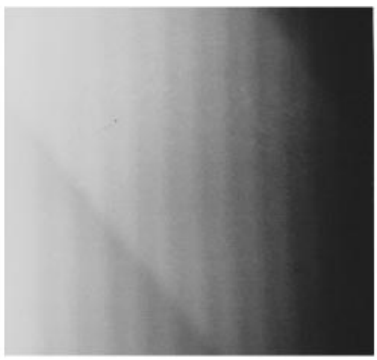

FIGURE 11. Steady, multicellular flow as visualized by: (*a*) particle-path time exposure for a 2.0 mm layer depth; (*b*) instantaneous shadowgraph with particles for a 1.5 mm layer depth; (*c*) thermograph for a 1.5 mm layer depth.

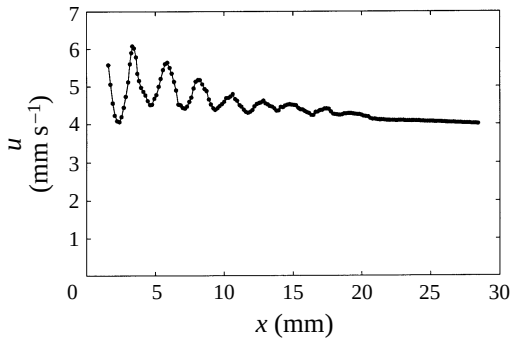

FIGURE 12. Horizontal velocity at $z/d = 0.9$ for steady multicellular flow in a 1.5 mm deep layer at $Ma = 800$.

However, the degree of smoothness of the results indicates that the observed increase is certainly not due to abrupt quantum changes in the number of cells in the apparatus.

3.4. *Oscillating multicellular flow*

If the steady multicellular flow states of §3.3 are driven vigorously enough by increasing the Marangoni number, a second transition will take place to a time-dependent

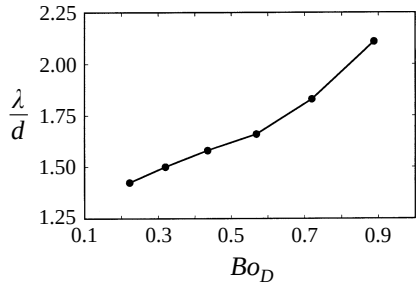

FIGURE 13. Dimensionless wavelength for steady multicellular states versus dynamic Bond number.

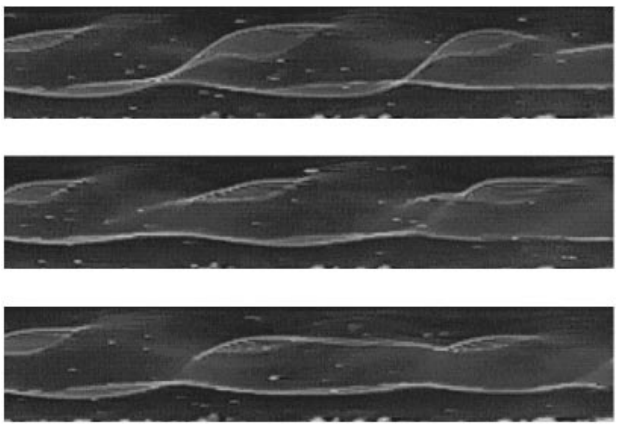

FIGURE 14. Instantaneous shadowgraphs at three instants of time (t is increasing from top to bottom) for the oscillatory multicellular state.

multicellular state. This state, although oscillatory, is not a pure travelling-wave state. This is evidenced by the sequence of shadowgraphs shown in figure 14, which shows the flow in a central portion of the apparatus. Time is increasing from top to bottom in the sequence, and the hot wall is to the left. Upon examining this sequence, there does not appear to be a well-defined wave speed associated with this state; there are pronounced differences between what is observed here and similar shadowgraphs for the pure hydrothermal-wave state of §3.2 (see Riley 1995). It is difficult to draw definite conclusions from such shadowgraph images, however, since the shadowgraph is integrated through the spanwise extent of the domain.

The free-surface thermograph shown in figure 15(*a*) provides greater insight into the structure of this flow. It is clear that there remain strong steady multicellular structures near the hot wall and a pair of oblique waves which appear to propagate through them, beginning at the cold wall. This is more evident in figure 15(*b*), in which data appearing in figure 15(*a*) have been enhanced through processing with an edge-finding filter, and subsequent binary windowing. A chevron pattern is observed near the cold wall which is suggestive of two interacting hydrothermal waves. In the absence of buoyancy, the nonlinear theory of Smith (1988) states that a single family should be observed (such as seen in figure 9) following instability of the pure return-flow basic state. However, the oscillatory instability observed here for large dynamic Bond numbers is reached from a different basic state (steady multicellular flow) than that considered by Smith, so his results are not strictly applicable. The

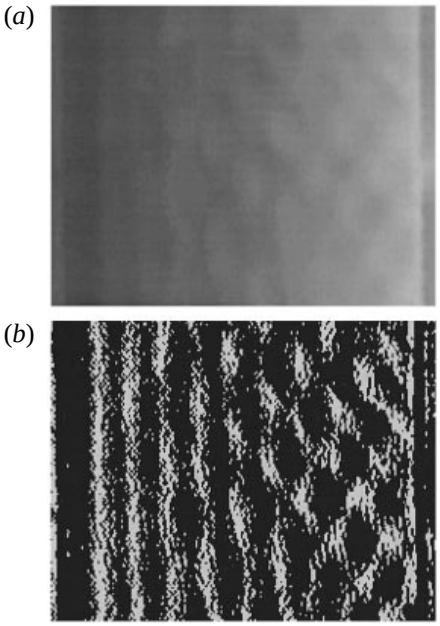

FIGURE 15. Instantaneous thermograph (*a*) and enhanced image (*b*) for the oscillatory multicellular state.

image shows that the steady multicells are still established at the hot wall, despite the vigorous oscillatory convection on the cold-wall side of the domain.

An oscillatory multicellular state is also observed by Schwabe *et al.* (1992) in a rectangular domain, but the reported results for that apparatus are sparse. They note, however, that a 1.8 mm deep layer of ethyl alcohol experiences a transition from a unicellular flow to a steady multicellular flow, and subsequently to a time-dependent flow at $Ma_L = 3000$. Villers & Platten (1992) make no attempt to examine the structure of their oscillatory flow states in acetone, but for their layer thicknesses ($d > 2.0$ mm, typically), the results of the present study strongly suggest that they are actually observing oscillating multicellular flow.

4. Discussion

Experiments have been conducted to investigate the hydrothermal-wave instability of thermocapillary convection in a thin liquid layer first predicted by Smith & Davis (1983). The results of these experiments offer the first conclusive laboratory proof of the existence of this instability; results of previous experiments conducted in deeper layers have been clouded by the presence of buoyancy, geometric effects, or both. Present results for $Bo_D = 0.080$ show a transition to oscillatory flow at a Marangoni number of $Ma = 324$, compared with the theoretical result (for a Prandtl number corresponding to the oil of these experiments) of $Ma = 295$ for $Bo_D = 0$; moreover, the results of figure 3 indicate that the experimental results asymptotically approach the theoretical limit as the Bond number decreases. The transition to hydrothermal waves from a state of steady unicellular flow (the core of which is shown to be an excellent approximation to the return-flow basic state of Smith & Davis), is a very sharp one.

In contrast, experiments performed with 'deep' layers do not experience a direct

transition from the return-flow basic state to oscillatory flow, but rather first exhibit a steady multicellular structure. Whether this state is the result of instability due to buoyancy or due to finite-geometry effects (e.g. such as the imperfect bifurcation of Taylor–Couette → Taylor-vortex flow in finite annuli) is still uncertain. While even the smallest streamwise aspect ratio ($L/d = 12$) encountered in these experiments is comparatively large, since the present apparatus does not permit changing the depth of the liquid layer without also modifying the aspect ratio of the flow domain, these results alone are insufficient to answer this question. Recently, Cramer, Schneider & Schwabe (1997) have proposed a mechanism for the appearance of multicellular structures which involves the deceleration of flow on the free surface and the establishment of an accompanying bulk-pressure distribution which stimulates the formation of multiple cells. Certainly, near the cold wall, such a rapid deceleration does occur in the present experiments (as shown in figure 6), but then one might question why the thinner of the two layers shown in figure 6 (with the higher deceleration) first transitions to a hydrothermal-wave state, rather than to a steady multicellular state. Additional numerical and laboratory experimentation is necessary to completely answer this question.

Increasing the Marangoni number from a state of steady multicellular flow ultimately results in the transition to time-dependent flow. In appearance, this flow resembles a pair of obliquely propagating hydrothermal waves riding on top of the steady multicellular flow. Since the primary aim of the present experiments was the characterization (and suppression, in Part 2) of the hydrothermal-wave instability, attention was restricted in the case of the oscillating multicellular state to the determination of the transitional Marangoni numbers shown in figure 3 and listed in table 1.

The authors wish to acknowledge helpful discussions with Professors D. F. Jankowski, M. K. Smith, A. Glezer & M. Schatz and the assistance of colleagues at the Microgravity Advanced Research and Support Centre in Naples, Italy and in the School of Physics at the Georgia Institute of Technology. This research was sponsored by the Microgravity Research Division within the Office of Life and Microgravity Sciences of NASA.

REFERENCES

Ben Hadid, H. & Roux, B. 1990 Thermocapillary convection in long horizontal layers of low-Prandtl-number melts subject to a horizontal temperature gradient. *J. Fluid Mech.* **221**, 77.

Benz, S., Hintz, P., Riley, R. J. & Neitzel, G. P. 1998 Instability of thermocapillary–buoyancy convection in shallow layers. Part 2. Suppression of hydrothermal waves. *J. Fluid Mech.* **359**, 165–180.

Chun, C.-H. & Wuest, W. 1979 Experiments on the transition from the steady to the oscillatory Marangoni-convection of a floating zone under reduced gravity effect. *Acta Astron.* **6**, 1073.

Cramer, A., Schneider, J. & Schwabe, D. 1997 On the transition from mono- to multiroll thermocapillary convection in shallow layers. *J. Fluid Mech.* (submitted for publication).

Daviaud, F. & Vince, J. M. 1993 Traveling waves in a fluid layer subjected to a horizontal temperature gradient. *Phys. Rev.* E **48**, 4432.

Davis, S. H. & Homsy, G. M. 1980 Energy-stability theory for free-surface problems: buoyancy-thermocapillary layers. *J. Fluid Mech.* **98**, 527.

De Saedeleer, C., Garcimartin, A., Chavepeyer, G. & Platten, J. K. 1996 The instability of a liquid layer heated from the side when the upper surface is open to air. *Phys. Fluids* **8**, 670.

Ezersky, A., Garcimartin, A., Mancini, H. L. & Perez-Garcia, C. 1993 Spatiotemporal structure of hydrothermal waves in Marangoni convection. *Phys. Rev.* E **48**, 4414.

Garr-Peters, J. M. 1992*a* The neutral stability of surface-tension driven cavity flows subject to buoyant forces–I. Transverse and longitudinal disturbances. *Chem. Engng. Sci.* **47**, 1247.

Garr-Peters, J. M. 1992*b* The neutral stability of surface-tension driven cavity flows subject to buoyant forces–II. Oblique disturbances. *Chem. Engng. Sci.* **47**, 1265.

Gatos, H. C. 1982 Semiconductor crystal growth and segregation problems on earth and in space. In *Materials Processing in the Reduced Gravity Environment of Space*. (ed. G. E. Rindone). Elsevier.

Kirdyashkin, A. G. 1984 Thermogravitational and thermocapillary flows in a horizontal liquid layer under the conditions of a horizontal temperature gradient. *Intl J. Heat Mass Transfer* **27**, 1205.

Levenstam, M. & Amberg, G. 1995 Hydrodynamical instabilities of thermocapillary flow in a half-zone. *J. Fluid Mech.* **297**, 357.

Mercier, J. F. & Normand, C. 1996 Buoyant-thermocapillary instabilities of differentially heated liquid layers. *Phys. Fluids* **8**, 1433.

Neitzel, G. P., Chang, K.-T., Jankowski, D. F. & Mittelmann, H. D. 1993 Linear-stability theory of thermocapillary convection in a model of the float-zone crystal-growth process. *Phys. Fluids* A **5**, 108.

Neitzel, G. P., Law, C. C., Jankowski, D. F. & Mittelmann, H. D. 1991 Energy stability of thermocapillary convection in a model of the float-zone crystal-growth process. II: Nonaxisymmetric disturbances. *Phys. Fluids* A **3**, 2841.

Parmentier, P. M., Regnier, V. C. & Lebon, G. 1993 Buoyant-thermocapillary instabilities in medium-Prandtl-number fluid layers subject to a horizontal temperature gradient. *Intl J. Heat Mass Transfer* **36**, 2417.

Preisser, F., Schwabe, D. & Scharmann, A. 1983 Verification of the oscillatory state of thermocapillary convection in liquid columns with free cylindrical surface. *J. Fluid Mech.* **126**, 545.

Riley, R. J. 1995 An investigation of the stability and control of a combined thermocapillary-buoyancy driven flow. PhD thesis, Georgia Institute of Technology.

Riley, R. J. & Neitzel, G. P. 1998 Linear-stability of buoyancy-thermocapillary convection in shallow layers. *in preparation*

Schwabe, D., Möller, U., Schneider, J. & Scharmann, A. 1992 Instabilities of shallow dynamic thermocapillary liquid layers. *Phys. Fluids* A **4**, 2368.

Schwabe, D., Scharmann, A., Preisser, F. & Oeder, R. 1978 Experiments on surface tension driven flow in a floating zone melting. *J. Cryst. Growth* **43**, 305.

Sen, A. K. & Davis, S. H. 1982 Steady thermocapillary flows in two-dimensional slots. *J. Fluid Mech.* **121**, 163.

Shen, Y., Neitzel, G. P., Jankowski, D. F. & Mittelmann, H. D. 1990 Energy stability of thermocapillary convection in a model of the float-zone crystal-growth process. *J. Fluid Mech.* **217**, 639.

Smith, M. K. 1986 Instability mechanisms in dynamic thermocapillary liquid layers. *Phys. Fluids* **29**, 3182.

Smith, M. K. 1988 The nonlinear stability of dynamic thermocapillary liquid layers. *J. Fluid Mech.* **196**, 391.

Smith, M. K. & Davis, S. H. 1983 Instabilities of dynamic thermocapillary liquid layers. Part 1. Convective instabilities. *J. Fluid Mech.* **132**, 119.

Velten, R., Schwabe, D. & Scharmann, A. 1991 The periodic instability of thermocapillary convection in cylindrical liquid bridges. *Phys. Fluids* A **3**, 267.

Villers, D. & Platten, J. K. 1992 Coupled buoyancy and Marangoni convection in acetone: experiments and comparison with numerical simulations. *J. Fluid Mech.* **224**, 487.

Wanschura, M., Shevtsova, S., Kuhlmann, H. C. & Rath, H. J. 1995 Convective instability mechanisms in thermocapillary liquid bridges. *Phys. Fluids* **7**, 912.